A Miniaturized Probe for Combined Two-Photon Microscopy and Femtosecond Laser Microsurgery

by

Christopher Luk Hoy, BSME

Thesis

Presented to the Faculty of the Graduate School of

The University of Texas at Austin

in Partial Fulfillment

of the Requirements

for the Degree of

Master of Science in Engineering

The University of Texas at Austin

December 2007

A Miniaturized Probe for Combined Two-Photon Microscopy and Femtosecond Laser Microsurgery

Approved by
Supervising Committee:

_____

_____

Dedication

This thesis is dedicated to my parents; for the limitless love, support, and encouragement, thank you. You are the best teachers and friends I could ask for. I also dedicate this thesis to my sister Lauren, who is a bigger nerd than I could ever hope to be.

Acknowledgements

The author would like to thank Dr. Adela Ben-Yakar for her guidance and for the opportunity to explore this interesting and rewarding area of research. The author would also like to thank the rest of the Ben-Yakar group for their assistance, support, and friendship; especially Nicholas Durr and Pengyuan Chen for assistance with the LabView® data acquisition program. The author would also like to thank the Solgaard group at Stanford University for supplying the MEMS device.

December 6, 2007

Abstract

A Miniaturized Probe for Combined Two-Photon Microscopy and Femtosecond Laser Microsurgery

Christopher Luk Hoy, MSE

The University of Texas at Austin, 2007

Supervisor: Adela Ben-Yakar

This thesis presents the design, fabrication, and characterization of a miniaturized two-photon fluorescence microscope system. The system is designed to act as a first step towards the design of a two-photon endoscope system capable of *in vivo* diagnostic imaging and delivery of high energy femtosecond laser pulses for microsurgery. Optical modeling software (TracePro®) was used to design a compact ($10 \times 15 \times 40$ mm^3) microscope system where field of view (FOV), resolution, and collection efficiency were identified as the key areas of performance. The resulting design utilizes two-axis gimbaled micromechanical system (MEMS) scanning mirror for laser scanning and air-core photonic crystal fiber for the delivery of femtosecond laser pulses. The system employs a miniaturized relay lens pair to limit aberrations due to pre-objective scanning and a separate, large numerical aperture fiber to enhance collection efficiency. The maximum FOV, lateral and axial resolution were measured to be 310 µm and 1.64 µm and 16.4 µm, respectively. The two-photon imaging capabilities of this miniaturized probe were demonstrated using fluorescent beads and pollen grains.

Table of Contents

List of Tables viii

List of Figures ix

Chapter 1: Introduction 1

1.1: Optical Imaging Modalities in the Biomedical Sciences 1

1.2: Two-Photon Microscopy for Cancer Detection and Diagnosis 5

1.3: Femtosecond Laser Microsurgery 7

1.3: Developments in Two-Photon Endoscopy 11

Chapter 2: Probe Design 14

2.1: Flexible Laser Delivery and Fluorescence Collection – Air-Core Photonic Crystal Fiber and Plastic Optical Fiber 15

2.2: Laser Scanning – MEMS Scanning Mirror and Relay Lenses 17

2.3: Focusing – Gradient Index Objective Lens 19

Chapter 3: Component Characterization 20

3.1: Component Characterization 20

3.2: Optical Modeling and Optimization 30

Chapter 4: Probe Construction 32

4.1: Physical Construction of the Miniature TPM/FLMS Probe 32

4.2: Data acquisition and Lissajous Scanning 34

Chapter 5: Probe Characterization 39

Chapter 6: Conclusion 44

References 47

Vita 51

List of Tables

TABLE 1. SUMMARY OF PUBLISHED TWO-PHOTON MICROSCOPY PROBES. 44

List of Figures

FIGURE 1.1.1 SIMPLIFIED JABLONSKI DIAGRAMS OF SINGLE-PHOTON AND TWO-PHOTON FLUORESCENCE. 3

FIGURE 1.1.2 A COMPARISON OF SINGLE-PHOTON AND TWO-PHOTON EXCITED FLUORESCENCE. 5

FIGURE 1.3.1. QUASI-FREE ELECTRON GENERATION DURING FEMTOSECOND LASER ABLATION. 9

FIGURE 2.1. BASIC LAYOUT OF THE COMBINED TPM/FLMS PROBE. 15

FIGURE 2.2.1. DIFFERENT LASER SCANNING PATTERNS FOR IMAGE RECONSTRUCTION. 17

FIGURE 3.1.1.1. INTERFEROMETRIC AUTOCORRELATION TRACES OF FEMTOSECOND PULSES BEFORE AND AFTER PROPAGATION THROUGH ONE METER OF AIR-CORE PCF. 21

FIGURE 3.1.1.2. PULSE DURATIONS BEFORE AND AFTER PROPAGATION THROUGH 1 METER OF AIR-CORE PCF. 22

FIGURE 3.1.1.3. BEAM PROFILES FOR THE COLLIMATED IMAGING AND MICROSURGERY BEAMS EXITING THE PCF. 23

FIGURE 3.1.2.1. THE GIMBALED TWO-AXIS MEMS SCANNING MIRROR DESIGN. 25

FIGURE 3.1.2.2. OPTICAL DEFLECTION OF THE MEMS MIRROR UNDER APPLIED DC VOLTAGE. 26

FIGURE 3.1.2.3. DYNAMIC SCANNING RESPONSE OF THE MEMS MIRROR BEFORE PACKAGING. 27

FIGURE 3.1.3.1. DEFINITION OF PITCH LENGTH IN A GRIN ROD LENS. 28

FIGURE 3.1.3.2. EXPERIMENTAL SETUP FOR CHARACTERIZATION OF GRIN OBJECTIVE LENS. 29

FIGURE 3.1.3.3. DETERMINATION OF THE GRIN LENS PSF. 30

FIGURE 3.2.1 RAY-TRACING MODEL OF THE MINIATURE TPM/FLMS PROBE SYSTEM. 31

FIGURE 4.1.1. SCHEMATIC AND PHOTOGRAPH OF THE COMBINED TPM/FLMS PROBE. 33

FIGURE 4.1.2. EXPERIMENTAL SETUP FOR THE COMBINED TPM/FLMS PROBE. 34

FIGURE 4.1.3. THE IMAGING MODES OF THE TPM/FLMS PROBE SOFTWARE.37

FIGURE 5.1. IMAGES OF FLUORESCENT BEADS USED TO CHARACTERIZE THE IMAGING CAPABILITIES OF THE TPM/FLMS PROBE. 40

FIGURE 5.2. TWO-PHOTON FLUORESCENCE IMAGES OF FLUORESCENTLY STAINED POLLEN GRAINS TAKEN WITH THE MINIATURIZED PROBE. 42

FIGURE 5.3. TWO-PHOTON FLUORESCENCE IMAGES OF BREAST CANCER CELLS LABELED WITH CALCEIN AM. 43

Chapter 1: Introduction

Femtosecond laser microsurgery has emerged as a remarkable technique for precise manipulation of biological systems with minimal damage to their surrounding tissues [1-3]. The combination of this technique with two-photon imaging, which has proven to be a versatile imaging tool [4-6], provides a non-invasive means of visualization to guide such surgery *in situ*. Though two-photon endoscopes have been built since 2001 [7-10], none have had surgical capabilities where the delivery of high peak intensity pulses presents new challenges. This thesis details a miniaturized probe built to act as a first step towards developing a combined two-photon microscopy and femtosecond laser microsurgery endoscope. The design of the probe will be discussed, along with the independent characterization of critical components. Finally, the construction and characterization of the imaging capabilities of the probe will be presented. Demonstration and characterization of the microsurgical capabilities are left for future study.

1.1: Optical Imaging Modalities in the Biomedical Sciences

Optical microscopy, including white light microscopy, fluorescence microscopy, and optical coherence tomography (OCT), maintains a vital role in medical diagnostics despite the advent of technologies such as X-ray, positron emission tomography (PET), computed tomography (CT), magnetic resonance imaging (MRI) and ultrasound. Though these imaging technologies are excellent for wide area and body-wide imaging, the enduring utility of optical microscopy is largely due to the modality's ability to provide real-time morphological information about a wide variety of tissues, often at low cost. This is in contrast to the alternative modalities described above, most of which require significant cost as well as time for creation and interpretation of a single image and are therefore of limited use for analyzing dynamic systems or providing intraoperative guidance.

Each of the optical microscopy modalities mentioned have their own unique advantages and drawbacks. Optical coherence tomography is an interferometric technique in which the light backscattered from the tissue is allowed to interfere with light from a reference arm and the resulting interference signal is detected. By moving the interference arm and scanning the light source along the surface of the sample, a three-dimensional (3D) image of the tissue can be created. Though OCT is capable of penetrating deep into to tissue, the reliance on scattered light for the detected signal means that OCT can only provide morphological information.

In contrast, fluorescence microscopy offers the potential to provide information beyond the morphological expression of a given tissue. In fluorescence microscopy, the tissue to be imaged is illuminated with light of a particular wavelength, and thus a particular photon energy. This photon energy corresponds to an electronic transition within certain molecules in the tissue, which causes an electron in the molecule to enter an excited state upon absorbing the photon, shown Fig. 1a. This excited electron relaxes nonradiatively to a slightly lower energy level in what is referred to as the Stokes shift, and then returns to its original state by emitting a new photon, referred to as fluorescence. This fluorescent light can be analyzed spectrally to gain spectroscopic information about the molecular fluorophores present in the tissue and/or collected through an imaging system which allows for the visualization of morphological features. Because of the Stokes shift, the excitation and emission photons are of different wavelengths, thus the excitation light can be filtered out to isolate the signal photons. Due to the wide-illumination of the sample used in fluorescence microscopy and spectroscopy, however, these imaging modalities lack any optical sectioning to allow axial distinction of tissue structures and provide little imaging depth.

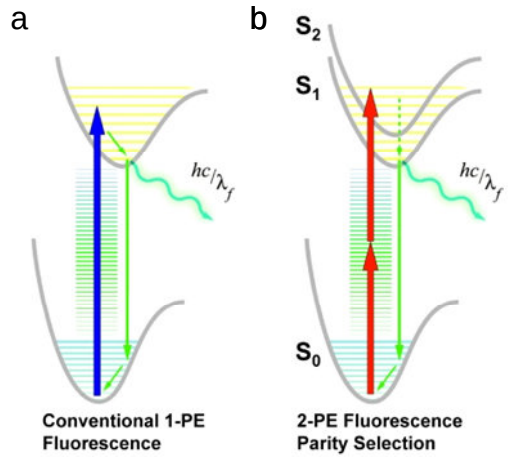

FIGURE 1.1.1 SIMPLIFIED JABLONSKI DIAGRAMS OF SINGLE-PHOTON AND TWO-PHOTON FLUORESCENCE. a, A diagram indicating the change in energy states during single-photon fluorescence. **b**, The same for two-photon fluorescence. Adapted from [11].

Optical sectioning in fluorescence microscopy can be achieved by scanning focused excitation light, most often but not necessarily laser light, on the sample and using a pinhole in the confocal plane of the emission collection optics. This is referred to as confocal microscopy, and the pinhole serves to block fluorescence emission arising from locations other than the focal volume. In practical terms, this means that the signal detected comes only from the lateral and axial location of interest, which allows for imaging beyond the surface of the tissue sample.

In 1990, the invention of two-photon fluorescence microscopy (TPM) took many of the advantages of confocal microscopy even further [4]. Two-photon fluorescence arises from the nonlinear interaction between light and matter at high peak intensities of the focused laser light. Here again, a ground-state electron is promoted to its excited state by the absorption of photon energy, shown in Fig. 1b. In this case, however, the incident light intensity is sufficiently high to cause the likely absorption of two photons

simultaneously, thus imparting twice the single-photon energy to the electron. The electron is then promoted to an excited state (governed by parity selection rules) and undergoes a similar Stokes shift and radiative decay observed in the case of single-photon fluorescence. Because two photons were absorbed instead of one, however, the individual photon energy used can be roughly half of what would be needed for single photon fluorescence, which corresponds to a longer wavelength excitation light. This means that the endogenous and exogenous fluorophores commonly excited with UV light in biological imaging can imaged using near infrared (NIR) light with two-photon microscopy.

Fluorescence excitation with NIR light affords several advantages over UV excitation. First, biological tissues are less attenuating at NIR wavelengths because both hemoglobin and water have low absorption coefficients. This creates what is often referred to as the "therapeutic window" for optical penetration of tissue and allows for deeper imaging than UV light can provide. Secondly, because the tissue and the fluorophore do not appreciably absorb NIR light, absorption only occurs when there is sufficiently high intensity to induce two-photon absorption, which can be seen in Fig. 2. This limits the region of fluorophore excitation to the focal volume, providing imaging of the tissue only at a specific depth and eliminating background signal from outside the focal volume. This provides optical sectioning of tissues samples similar to the pinhole used in confocal, but without rejecting any of the fluorescent emission as is done by the pinhole, while the decreased out-of-plane absorption allows for deeper imaging than confocal microscopy [12]. The lack of out-of-plane absorption also serves to reduce photodamage effects in these areas when compared to single photon excitation.

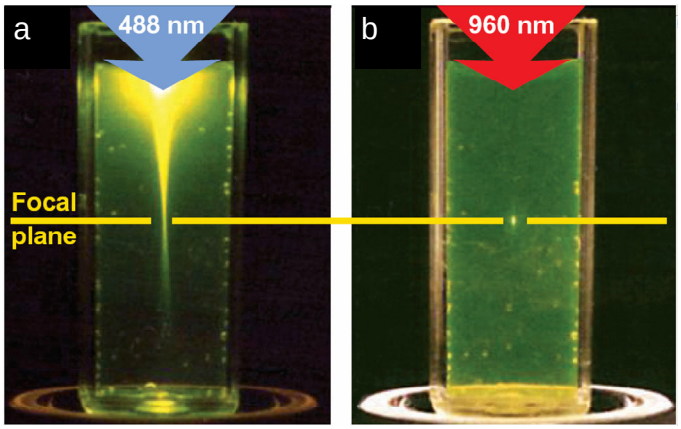

FIGURE 1.1.2 A COMPARISON OF SINGLE-PHOTON AND TWO-PHOTON EXCITED FLUORESCENCE. Note the out-of-plane fluorescence generated during single-photon excitation in **a** compared to two-photon excitation in **b**, where the signal is generated only within the focal volume. Reproduced from [6].

As a result of these advantages, numerous biomedical applications for TPM have arisen. In neuroscience, TPM has been found attractive for its combination of high resolution and minimized out-of-focus photodamage and has been used *in vivo* to observe axons and dendritic activity in the brain tissue of anesthetized mice [7, 13, 14]. Similarly, the technique has proven useful for providing architectural and dynamical information about tissue vasculature [7, 15, 16]. Among the prospective biomedical applications for TPM, the use of the technique for early detection and diagnosis of cancer is of particular interest with TPM already proving useful in this role.

1.2: TWO-PHOTON MICROSCOPY FOR CANCER DETECTION AND DIAGNOSIS

Recently, researchers have demonstrated that healthy, precancerous and cancerous cells can be differentiated with TPM of endogenous fluorophores, a process often referred to as autofluorescence [17-20]. In these studies, TPM has proven to be effective for positively identifying cancerous cells within bulk tissue using numerous different indicators. For example, Skala *et al*. [19] utilized well known morphological indicators

in combination with changes in signal intensity to differentiate neoplasia and carcinoma *in situ* from normal healthy tissue. Additionally, by combining TPM with fluorescent lifetime imaging techniques, Leppert *et al*. [20] and Skala *et al.* [21] showed that tumor tissue could be distinguished from healthy tissue by the two-photon-excited fluorescence lifetime of the native fluorophores, which resulted in stunning contrast of healthy and diseased tissue at the interface.

In addition to the detection of cancerous lesions, recent studies have also proposed novel ways in which TPM could provide information on cancer staging as well. One method of cancer staging being explored is the use of TPM to map the vasculature and angiogenesis of tumors [22]. By using fluorescent labels, researchers have been able to map out the vascular system of tumors and thus determine the degree of angiogenesis, a clear marker of tumor progression. Due to the combined high resolution and fast imaging speed of TPM, several groups have also been able to track molecular kinetics and blood flow rates through these vascular systems, giving an indication of which areas of the tumor are growing fastest [16, 17]. Studies have also demonstrated the use of TPM in imaging various markers indicating gene expression in cancerous tissue, which (in addition to blood flow) can tell physicians whether a cancer would respond to certain chemotherapy or radiological treatments [17].

One criticism of TPM and of optical microscopy in general is that these modalities generally only provide localized, "skin-deep" imaging. In the case of TPM, the fields of view are generally constrained to sub-mm^2 areas and depths are limited to about 1-2 mm depending on the optical properties of the tissue. However, more than 85% of all cancers originate in the epithelium, which is the thin layer of tissue that serves as a barrier between the inside of the body and either the outside world or internal body cavities, such as the lungs and gastrointestinal tract [23]. As cancerous lesions grow,

they can burst through the basal membrane and gain access to the blood stream for nourishment and an entrance to the rest of the body. This makes early detection of cancerous and precancerous lesions inside the epithelium extremely important to the fight against cancer. Fortunately, even in the thickest epithelial tissue, the stratified squamous epithelium of the skin, the epithelial layer thickness is limited to a few hundred microns, making the entire tissue structure accessible to TPM. In addition to early cancer detection, TPM could be used intraoperatively to analyze tumor margins *in situ*. Because TPM can provide real-time information about tissue structures, surgeons could potentially use TPM during tumor excisions to determine if all of the cancerous tissue has been removed, eventually eliminating the time consuming process of biopsy and limiting the need for successive surgeries. By combining reliable diagnosis and staging in a relatively quick procedure, TPM has great potential as a screening tool for suspicious lesions in high risk areas such as the cervix and colon; as an intraoperative tool for margin determination; and as a minimally invasive and high-resolution guidance tool for neuro-oncology. If this potential diagnostic tool were paired with an equally precise means for surgery, this technology could be taken further still and give rise to a new class of high precision "seek-and-treat" medical endoscopes. This level of surgical precision can be achieved using high-intensity ultrashort pulses for femtosecond laser microsurgery (FLMS).

1.3: FEMTOSECOND LASER MICROSURGERY

Traditionally, the lasers used for surgical procedures have been continuous wave (cw) or pulsed lasers with pulse durations longer than 1 ns. These lasers rely on a linear heating mechanism to damage and cut tissue. Despite advantages over conventional surgery for certain applications, the thermal damage mechanism leads to collateral cell damage due to the dissipation of heat within the targeted tissue. In contrast, the damage

from femtosecond pulses in tissue is understood to be the result of optical breakdown via rapid generation of a small confined plasma. In this model, the energy is deposited in the sample in the femtosecond timescale, leading to the rapid ionization of the sample in less than the thermal or acoustic relaxation times [3]. Without linear heating and extensive thermal dissipation, femtosecond lasers can ablate tissue with two to three orders of magnitude less energy than with nanosecond-pulsed lasers, which leads to less collateral damage to surrounding cells.

In the optical breakdown process, the high intensity of the incident electric field creates quasi-free[1] electrons in the conduction band through multiphoton ionization and tunneling, as illustrated in Fig. 1.3.1. These free electrons can then gain kinetic energy through a series of inverse bremsstrahlung collision events and then generate more free electrons through impact ionization [24, 25]. This cycle can continue, creating an increasing number of free electrons in what is referred to as avalanche ionization. Although, because inverse bremsstrahlung and subsequent impact ionization rely on a series of collision events, recent comparison of the predicted collision frequency and pulse duration imply that avalanche ionization, while still significant, might not be as dominant as once thought [24, 26].

[1] For simplicity's sake, electrons that have been promoted to the conduction band will henceforth be referred to as "free" electrons in this work.

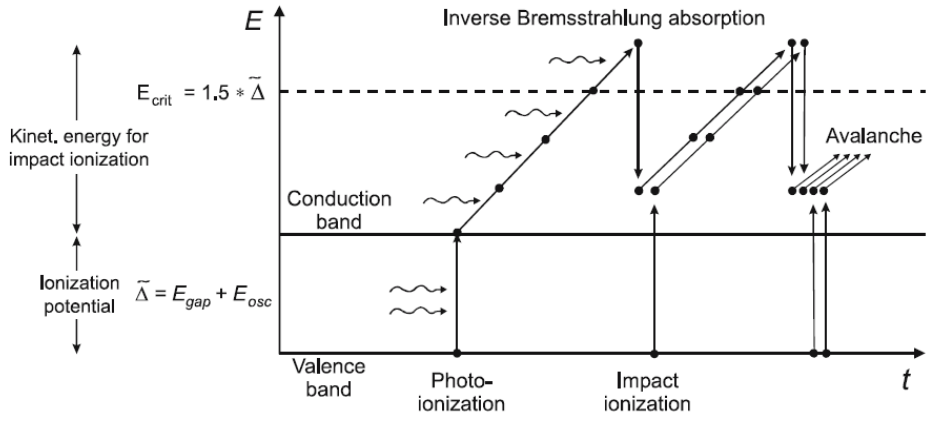

FIGURE 1.3.1. QUASI-FREE ELECTRON GENERATION DURING FEMTOSECOND LASER ABLATION. Seed electrons are promoted into the conduction band through a combination of multiphoton ionization and tunneling; they then give rise to avalanche ionization which rapidly increases the number of conduction-band electrons. Reproduced from [3].

The generation of free electrons results in the formation of a plasma, with the commonly accepted optical breakdown limit defined as when the plasma reaches a critical electron density, taken to be 10^{21} cm^{-3} for a laser wavelength of 800 nm. At this point the plasma becomes highly absorbing and reflective, and can shield much of the subsequent radiation. The highly localized plasma creates a confined region of high temperature and tensile stress which results in vaporization of the material within focal volume [27]. Because the process does not rely on linear absorption, the laser wavelength can be chosen in the NIR region, or in the "therapeutic window", as for TPM. As a result, FLMS can be used to cut deep into tissue without harming superficial cells. This makes femtosecond laser ablation an extremely attractive tool for nanosurgery, as the damage effects are highly localized and consistent across different structures.

Plasma-mediated femtosecond ablation has been demonstrated in a number of biological applications. For example, Shen *et al*. and Watanabe *et al*. both used NIR femtosecond pulses to disrupt individual mitochondrion within a living cell [28, 29]. In both studies, ablation of a single spot on a mitochondrion was shown to have destroyed the organelle while leaving neighboring organelles, and the entire cell, intact. In addition, several research groups have demonstrated the ability form transient pores in the plasma membrane that can be used to aid cellular uptake of fluorescent dyes or foreign DNA without compromising the viability of the cell [1, 28, 30]. Perhaps foreshadowing promising neurobiological applications for FLMS, a recent study has also demonstrated femtosecond laser nanoaxotomy, in which individual axons were severed with a femtosecond laser with sufficient precision to observe subsequent axonal regrowth [2, 31].

In addition to femtosecond laser ablation using high intensity amplified pulses, it is also possible to conduct microsurgery using higher pulse energies at 80 MHz repetition rate directly from a laser oscillator normally used for imaging. For example, several studies have shown a much lower damage threshold for microtubules, in which the breaking of a single bond can lead to depolymerization of the fibers due to the dynamic instability inherent to this structure [32, 33]. Also, femtosecond laser pulses can create photochemical reactions leading to the creation of reactive oxygen species, which degrade many biological molecules, including DNA, and can in turn lead to cell death [33]. While these examples demonstrate an alternative method of femtosecond laser microsurgery, they rely on the biochemistry of their target for photodamage in contrast to the deterministic plasma-mediated ablation caused by high intensity femtosecond laser pulses.

It is important to note, however, that FLMS with high intensity laser pulses can prove difficult in deep tissue, where increased scattering requires increased laser pulse energy. This increase in energy can lead to self-focusing, which occurs when the peak intensity of the pulse is high enough to increase the nonlinear index of refraction, resulting in a "lensing" of the tissue which focuses the pulse. The result is that ablation begins prior to reaching the normal focal volume. In some cases, the pulse energy may be high enough to also generate a low density plasma, which will counteract the self-focusing through plasma defocusing and cause the pulse to propagate as a filament, modifying the tissue in a streak along the optical axis [34]. Both effects need to be avoided and may be mitigated by using high numerical aperture (NA) focusing optics and by operating close to the threshold energy for ablation.

With this caveat, FLMS offers unrivaled precision and would be invaluable in many delicate clinical procedures, such as the removal of diseased cells in brain tissue or the elimination of small cancerous lesions in sensitive locations. A tool of this precision, however, is wasted without an equally precise means for visualization, guidance, and control. Due to their complimentary properties and similarity in laser systems, TPM is a logical choice to combine with FLMS for clinical applications. While this has been accomplished in laboratory settings in large table-top systems, so far this technology has not been developed for the clinical setting [30, 32]. By combining both techniques within a small and flexible housing, the all-optical "seek-and-treat" endoscope can become reality.

1.3: DEVELOPMENTS IN TWO-PHOTON ENDOSCOPY

In 2001, Helmchen *et al*. reported the development of a miniaturized two-photon fluorescence microscope that could be mounted on the head of freely moving mice to observe brain activity [7]. Since then, several other miniature TPM devices have been

developed for neurological research [9, 35, 36] and recently also towards clinical examination of diseased tissue [10, 37], all of which have slightly different approaches though similar goals.

For most biomedical applications, the key figures of merit for an imaging device are the imaging resolution, the maximum viewable area or field of view (FOV), the imaging speed, and the overall device size. All miniature TPM probe designs thus far, save the device in Helmchen *et al*., have utilized gradient index (GRIN) objective lenses, to be discussed in detail later, which can provide single micron level resolution. There exist wide variations, however, in both the FOV and imaging speed among the current devices. In FOV, the range spans between 320 µm in diameter for the fiber-bundle probe of Göbel *et al*. to 80 µm × 20 µm for the MEMS-based device of Piyawattanametha *et al.*, and the variation is largely due to differences in beam scanning methods [35, 38]. Generally speaking, TPM probes can utilize either a proximal scanning of the laser outside of the probe housing, such as through a fiber bundle [35], or a method of distal scanning utilizing a miniaturized scanning device inside of the probe itself, most notably through scanning of the fiber tip [7, 9, 37] or, recently, through a microelectromechanical systems (MEMS) device [10, 38]. Each method has distinct advantages and disadvantages and will be discussed in greater detail later. The size of TPM probes vary depending on the device's purpose and mode of insertion. Recently, probes have been developed with outer tool diameters less than 5 mm, most notably by Fu *et al*. [10], which is generally the largest diameter tool or accessory channel found in commercial endoscope housings and is considered a requisite for internal medicine use.

Despite the advances in miniaturized and portable TPM systems described above, all of the devices mentioned are merely observation tools without the ability to manipulate the images they see. By combining TPM and FLMS techniques within a

small portable probe, the ultrafast laser can be taken beyond passive imaging to create a novel “seek-and-treat” tool for all-optical diagnostics and therapeutics. This thesis presents the design and construction of such a combined TPM/FLMS probe, intended as a first step towards development of an endoscope-ready clinical device.

Chapter 2: Probe Design

In designing a versatile miniature imaging and microsurgery system with an eye on future clinical development, several key design criteria were identified. Namely, such a device requires a large field of view relative to the features under investigation, sub-cellular resolution, high imaging speed for real-time feedback, efficient light collection for weak signals, and an ability to deliver high-intensity microsurgery pulses with minimal distortion. In addition, the delivery of ultrashort laser pulses via optical fiber and miniaturized optics presents several design challenges, many of which are exacerbated when amplified ultrashort pulses are needed. The most common problem is that of group velocity dispersion (GVD), wherein the pulse duration increases as the pulse propagates through an optical element. As the emitted fluorescent signal depends inverse linearly on the pulse duration [39], GVD must be minimized to achieve the maximum fluorescent signal.

As mentioned in the previous chapter, the imaging characteristics listed above are heavily dependent on the choice of components such as laser delivery fiber, scanning mechanism, and objective lens, all of which must be designed to handle the delivery of high peak intensity ultrashort laser pulses. To better understand the role each of these components would play in a fully miniaturized endoscope, a small probe was designed to act as a miniature optical table or test bench in which components could be tested without the packaging concerns of a clinical microendoscope. In this design, shown in Fig. 2.1, an air-core fiber would deliver both unamplified femtosecond pulses at 80 MHz repetition rate from a Ti:Sapphire oscillator for imaging and amplified pulses at 1 kHz from a chirped pulse amplification (CPA) system for microsurgery. The laser beam would then be scanned by a gimbaled two-axis MEMS scanning mirror through a

miniature relay lens pair which would image the laser light from the MEMS mirror to the back aperture of a miniature GRIN objective lens. A dichroic mirror would separate the excitation and emission light with the emitted fluorescence being collected by a large core, large NA plastic optical fiber. This chapter will discuss each component and their benefits for use in a miniature TPM/FLMS probe.

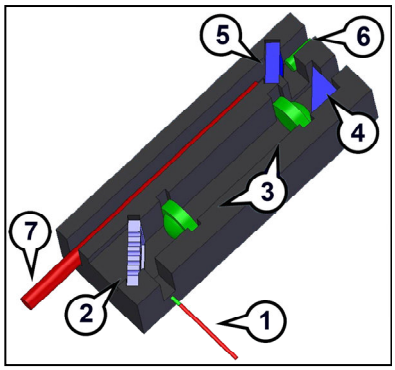

FIGURE 2.1. BASIC LAYOUT OF THE COMBINED TPM/FLMS PROBE. The design consists of 1) an air-core fiber, 2) two-axis MEMS scanning mirror, 3) miniature aspheric relay lenses, 4) mirror, 5) dichroic mirror, 6) GRIN objective lens, and 7) large core plastic optical fiber.

2.1: FLEXIBLE LASER DELIVERY AND FLUORESCENCE COLLECTION – AIR-CORE PHOTONIC CRYSTAL FIBER AND PLASTIC OPTICAL FIBER

Flexibly decoupling the miniature probe from the optical table requires the use of fiber optics for delivery of the laser light and collection of the fluorescent emission. Though Helmchen *et al.* [7] succeeded in utilizing a miniature photomultiplier tube (PMT) in their probe, the current sizes of such devices prevent their use in a clinical endoscopy application. The dominant source of GVD in miniaturized two-photon microscopes is often the optical fiber used to deliver the femtosecond pulses. In the case of traditional single-mode fiber, significant GVD can be expected after less than 10 cm of

propagation, making the use of such fibers without pre-chirping impractical [36]. For amplified pulses this problem worsens with the onset of self-phase modulation (SPM), which broadens the spectral bandwidth of the pulses and leads to increased GVD.

To avoid these problems, we have utilized an air-core photonic crystal fiber (PCF), examples of which have been successfully demonstrated to deliver ultrashort pulses with pulse energies as high as 1 µJ and over distances exceeding 25 m [40]. Air-core PCF accomplishes this by confining light within a photonic bandgap structure which consists of a series of regularly spaced holes within a dielectric (silica) with a central defect (the core). Light of certain wavelengths, dictated by the hole spacing, is forbidden to propagate perpendicularly through the holey structure and is thus confined to the core. By confining light in this manner and eschewing the total internal reflection principal used by standard fibers, the core can be made of a very low index material, which in this case is air. Air has a very low material dispersion and nonlinear index of refraction, and as the air-core PCF is inherently single-mode, it makes an attractive candidate for delivery of amplified ultra-short pulses.

Although adept at delivery of high intensity laser pulses, air-core PCF is a less than ideal candidate for collection of fluorescence emission. This is because the small core size (approximately 5 – 10 µm) and NA (approximately 0.15 – 0.20) are ill-suited to coupling scattered light and the photonic bandgap is non-guiding at emission wavelengths. For this reason, a separate collection fiber with a large NA was chosen. This allows for a separate optical pathway that can be fully optimized for the collection of scattered light instead of the delivery of high intensity laser light. For this purpose, a plastic optical fiber was chosen which possesses a core size of 2 mm and a NA of 0.51.

2.2: LASER SCANNING – MEMS SCANNING MIRROR AND RELAY LENSES

As mentioned earlier, beam scanning in miniaturized TPM systems has generally been achieved through proximal scanning of a coherent fiber bundle, or distal tip scanning using the laser-delivery fiber or a MEMS scanning mirror. Though proximal scanning eliminates the need for miniaturization of the scanning device, coherent fiber bundles inherently limit resolution to the fiber core spacing in the bundle. In addition, the low NA and small core size of air-core PCF limits the efficiency of scanned coupling into a bundle of these fibers. While fiber-tip scanning has been implemented since the earliest TPM probe designs, this scanning method can lead to off-axis aberrations due to the scanning of diverging light. Gimbaled two-axis MEMS mirrors, such as described in Lee *et al*. [41], can provide optical scanning angles in excess of 10º and can be used to scan the laser beam in either a raster scan or Lissajous scan, illustrated in Fig. 2.2.1.

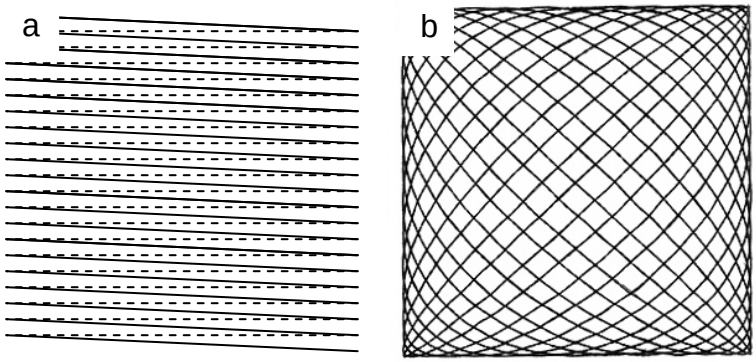

FIGURE 2.2.1. DIFFERENT LASER SCANNING PATTERNS FOR IMAGE RECONSTRUCTION. Many two-photon microscopes, including our table-top system, scan the laser in a raster pattern, shown in **a**. In this pattern as it is shown here, the horizontal axis moves very rapidly while the vertical axis moves slowly at the frame rate. Alternatively, Lissajous scanning, **b**, moves both axes sinusoidally to cover the FOV, resulting in a mesh pattern. Note that in the Lissajous scan, the outside is scanned more than the inner portions of the FOV and specific points are scanned repeatedly in a frame.

The raster scanning pattern is common among laser scanning microscopes and scans the laser beam line by line, collecting information in rows. With a MEMS mirror, this requires one scanning axis to be moved slowly (approximately at the frame rate), with one of the MEMS axes driven far off of resonance, and the other axis to be driven fast to maximize imaging speed. Currently, all published miniature TPM systems utilizing MEMS scanning devices make use of a raster scan, although the limited off-resonance deflection ultimately limits the attainable FOV [10, 38, 42]. Alternatively, the laser can also be scanned by driving both mirror axes at resonance. When both axes simultaneously move along sinusoidal trajectories, a Lissajous scanning pattern can be created. By exciting the resonant frequencies of the MEMS mirror, large scanning angles can be achieved using relatively low driving voltages, although image reconstruction is more difficult than in the raster pattern. Lissajous patterns have been implemented in fiber-tip scanning miniature TPM systems, where the piezoelectric devices used to drive the fiber tips have poor off-resonance scanning characteristics. In addition, Dickensheets *et al.* implemented a Lissajous scan using a MEMS scanning mirror in a miniature confocal microscope over a decade ago [43].

When used in conjunction with the relay lens pair, the laser can be scanned throughout the full range of the mirror's deflection without movement of the beam from the back aperture of the objective lens. This minimizes aberrations while maximizing the FOV of the system and ensures a flat focal plane at the sample. In addition, the relay lens pair can act as a telescope so that the laser beam waist can be small at the MEMS to maximize power delivery and fill the back aperture at the objective to maximize NA and optimize resolution. One popular solution for a relay lens system in two-photon endoscopy design has been to utilize multi-pitch GRIN lenses [36]. Though easily packaged in small sizes, such lenses have multiple internal focal points which can lead to

self-phase modulation and even material damage when used with high intensity femtosecond pulses for surgery. Due primarily to this constraint, individual miniature aspherical lenses were chosen for the relay lenses in the probe.

2.3: FOCUSING – GRADIENT INDEX OBJECTIVE LENS

The objective lens options for a miniaturized TPM system are limited, given the small sizes of the systems. A suitable lens must balance high numerical aperture, for efficient fluorescent excitation and collection, small diameter, and sufficient working distance. These criteria are equally important for FLMS systems as well. The most common solution thus far has been to use a GRIN rod lens, which are readily available with diameters down to 0.5 mm. As the name implies, lenses of this sort use a gradient in their refractive index to focus light, rather than curvature of the surfaces, and can achieve NAs up to ~0.6 with working distances of several hundred microns. This theoretically provides these lenses with the ability to resolve sub-micron level features and image through the entire epithelial tissue layer. Though aberrations often prevent the lens from achieving this level of performance in practice and will be discussed later, the compact size and availability of such lenses make them a suitable choice for a miniaturized TPM/FLMS system.

Having determined the components needed for a miniature TPM/FLMS probe system, it was necessary to specify each component and characterize their performance to arrive at a final design.

Chapter 3: Component Characterization

To better understand the contribution of each component to the imaging capabilities of the TPM/FLMS probe, critical components were first characterized separately. This independent characterization of each component also provided benchmarks in resolution and scanning angle, for example, which could be expected under ideal conditions in the fully miniaturized system. This benchmark data was then used in conjunction with a ray-tracing optical model of the system to provide predictions of the overall probe performance.

3.1: COMPONENT CHARACTERIZATION

3.1.1: Photonic Crystal Fiber

As previously noted, the multiphoton absorption mechanism at the heart of TPM and FLMS is sensitive to pulse duration. Though the air-core PCF propagates the laser light through air and thus introduces extremely low material dispersion, waveguide dispersion is still present and can introduce significant anomalous dispersion to the pulse. As a result, laser pulses far from the minimally dispersive wavelengths of the fiber can be increased by an order of magnitude or more during propagation through one meter of PCF.

The air-core PCF (air-6-800, Crystal Fibre A/S) employed in our miniature TPM and FLMS system has a transmission range from 750 nm to 800 nm, and a zero-dispersion wavelength at approximately 755 nm, above which the fiber is anomalously dispersive. We characterized the pulse duration for both the imaging and microsurgery laser pulses by analyzing the pulse duration before and after propagating through the fiber.

We used a homebuilt interferometric autocorrelator (utilizing a GaAsP photodiode as a nonlinear signal transducer [44]) to measure the pulse durations before and after propagation through the fiber, as seen in Figs. 3.1.1.1 and 3.1.1.2. The autocorrelation measurements supported the experimentally determined dispersion curve when accounting for the dispersion introduced from the objective lens, and agreed with the manufacturer's dispersion specifications.

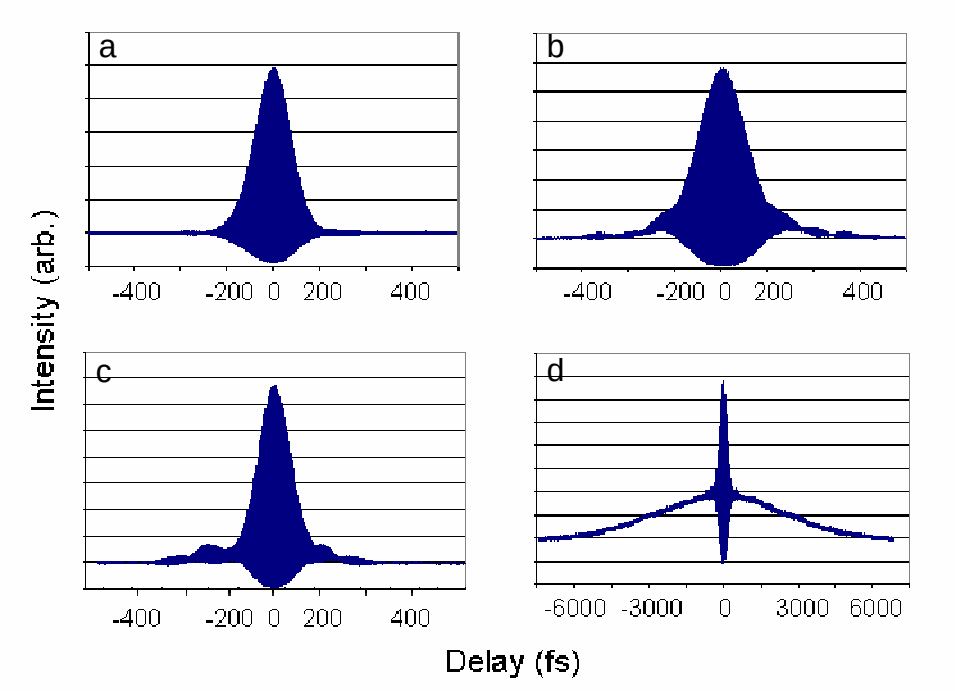

FIGURE 3.1.1.1. INTERFEROMETRIC AUTOCORRELATION TRACES OF FEMTOSECOND PULSES BEFORE AND AFTER PROPAGATION THROUGH ONE METER OF AIR-CORE PCF. **a** and **b** are autocorrelation traces at 753 nm center wavelength before and after the fiber, respectively. The pulse durations measured are 117 fs and 152 fs, respectively. **c** and **d** are traces at 780 center wavelength before and after the fiber with pulse durations of 142 fs and 3.2 ps, respectively. The "wings" on **d** are indicative of a heavily chirped pulse, in which the blue-shifted pulse front does not interfere as well with the red-shifted pulse tail (for the case of anomalous dispersion).

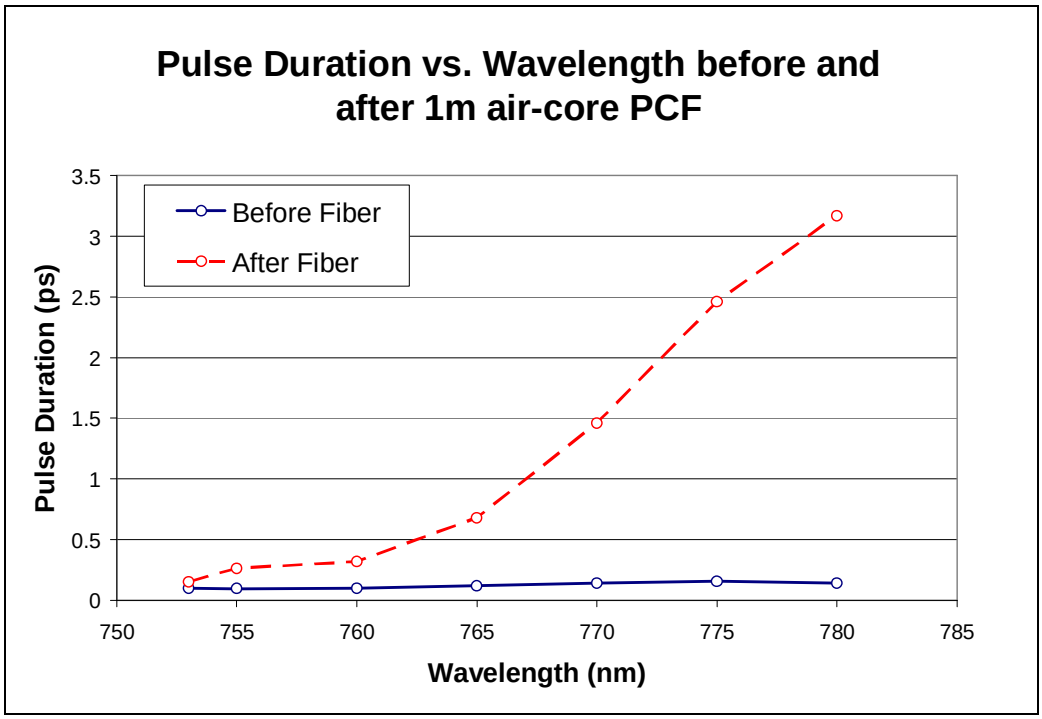

FIGURE 3.1.1.2. PULSE DURATIONS BEFORE AND AFTER PROPAGATION THROUGH 1 METER OF AIR-CORE PCF. The pulse duration was measured by the homebuilt interferometric autocorrelator before (blue) and after (red) the fiber.

For the microsurgery beam, the wavelength is not easily tunable and is optimized at 780 nm, where the fiber is highly dispersive. To compensate for this, the path difference delays in the pulse compressor of the chirped pulse amplifier (CPA) were decreased to leave a degree of positive chirp in the output pulse. To optimize the pulse dispersion compensation, the laser pulses were coupled into the fiber and then focused onto a photodiode (G1117, Hamamatsu) which exhibits two-photon absorption in the NIR. The signal from the photodiode was then maximized by changing the path delay inside the compressor of the CPA. Using the homebuilt autocorrelator, the pulse duration at the exit of the fiber was measured to be 178 fs.

In addition to dispersion characterization, a beam profiler (Spiricon LBA-PC with UNIQ UP-680-12B camera) and spectrum analyzer (Ocean Optics USB2000) were used to ensure the output beams were single mode and exhibited no spectral broadening for input pulse energies up to 2 µJ. The laser beam from the Mai Tai oscillator was delivered through 1 meter of photonic crystal fiber and collimated by a 0.46 NA GRIN lens. The subsequent beam profiles for the collimated laser beam at 760 nm and 780 nm center wavelength and at various distances along the propagation axis are provided in Fig. 3.1.1.3. These two wavelengths were chosen to be representative of the wavelengths predicted for use during imaging and microsurgery experiments. The collimated beam width emerging from the collimating lens was found to be 366 µm and 440 µm for 760 nm and 780 nm, respectively, while their far field divergence angles were measured to be 0.076° and 0.075°, respectively.

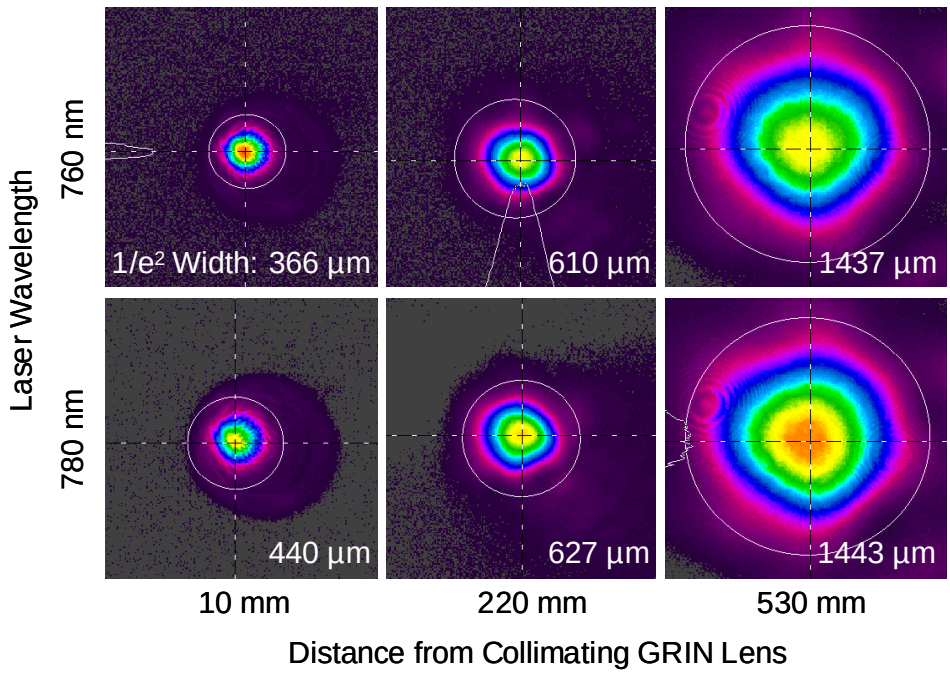

FIGURE 3.1.1.3. BEAM PROFILES FOR THE COLLIMATED IMAGING AND MICROSURGERY BEAMS EXITING THE PCF. The $1/e^2$ beam widths were measured

using the beam profiling software and were used to calculate far-field divergence angles to confirm suitable collimation.

The expected divergence for a collimated single-mode (Gaussian) beam is given by

$$\theta = \frac{\lambda}{\pi w_0} \qquad (1)$$

where θ here is the far field divergence half angle, λ is the center wavelength of the propagating laser light, and w_0 is the minimum beam radius. For the measured beam waists indicated above, we calculated that the theoretical far field divergence angles for collimated Gaussian beams (0.076° and 0.065° at 760 and 780 nm, respectively) agree well with the measured values of 0.075° and 0.076° at 760 and 780 nm, respectively. This study indicates that the light emerging from the fiber is well collimated and is in a Gaussian TEM_{00} mode.

3.1.2: MEMS Scanning Mirrors

The particular MEMS device implemented in our miniature TPM/FLMS system has a bare Si mirror measuring 500 × 500 μm^2 and was provided by our collaborators at the Solgaard group at Stanford University [41]. The device, illustrated in Fig. 3.1.2.1, operates using banks of vertical combs, which are driven outward by electrostatic forces. This creates torsion on along the mirror support, which twists the mirror along this axis. By fabricating the mirror on an inner and an outer axis in a gimbaled fashion, the mirror can rotate in two decoupled and orthogonal directions.

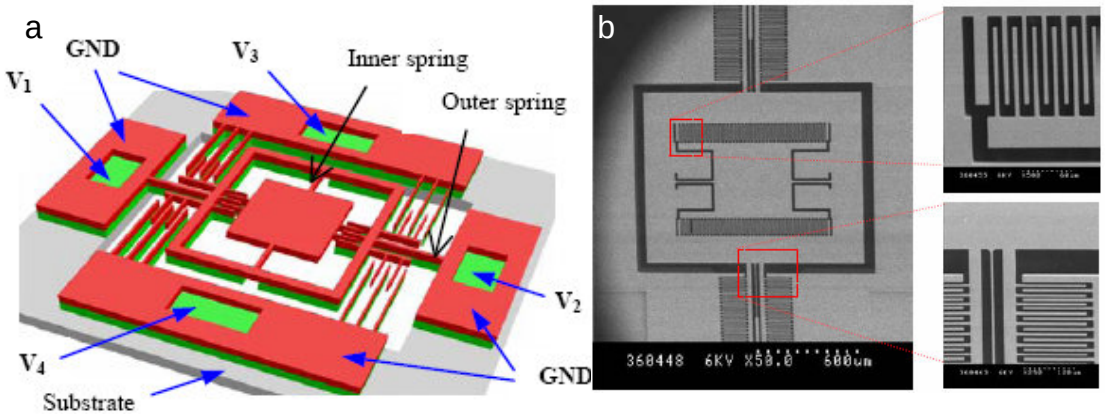

FIGURE 3.1.2.1. THE GIMBALED TWO-AXIS MEMS SCANNING MIRROR DESIGN. An illustration, **a**, of the scanning mirror structure shows the general layout of the voltage connections and rotating axes of the mirror. A scanning electron micrograph of a device similar to the one used in the probe is shown in **b**, where the insets show detail of the vertical comb structures used to drive the mirror. Reproduced from [41].

To facilitate characterization of the MEMS scanning mirror, the silicon-on-insulator chip containing the device was provided on a 40-pin dual in-line package (DIP) chip. The chip was then mounted to a breadboard and illuminated with a helium-neon laser. By observing the reflected laser light on a wall 2.5 meters away, the deflection of the beam could be measured during actuation of the MEMS mirror.

Though scanning mirrors sharing the design of our device have been shown to exhibit static optical deflections in excess of ±7°, defects limited the static deflections of our device to less than ±1° on the inner axis and negligible deflection on the outer axis, as seen in Fig. 3.1.2.2.

Dynamic scanning of the mirror was achieved by applying a sinusoidal voltage signal between zero and some peak voltage with opposing comb banks driven 180 degrees out of phase. In this manner, the device could be driven to large deflections by exciting the resonant frequencies of the two axes. Shown in Fig. 3.1.2.3, the resonant

frequencies of the outer and inner axes of the mirror were measured to be 1.54 kHz and 2.73 kHz, respectively. The maximum beam deflection at resonance was measured to be ±13.9° and ±7.6° for the outer and inner axes with 57 V peak driving voltage to both axes. After transferring the device to a 7 mm × 9 mm leadless chip carrier for packaging inside the probe housing, however, the measured deflection at resonance had decreased to ±10.5° and ±10.0° for the outer and inner axes, respectively, using 80 V peak driving voltage to both axes. The maximum beam deflection of MEMS mirror on a chip carrier was measured outside the probe housing.

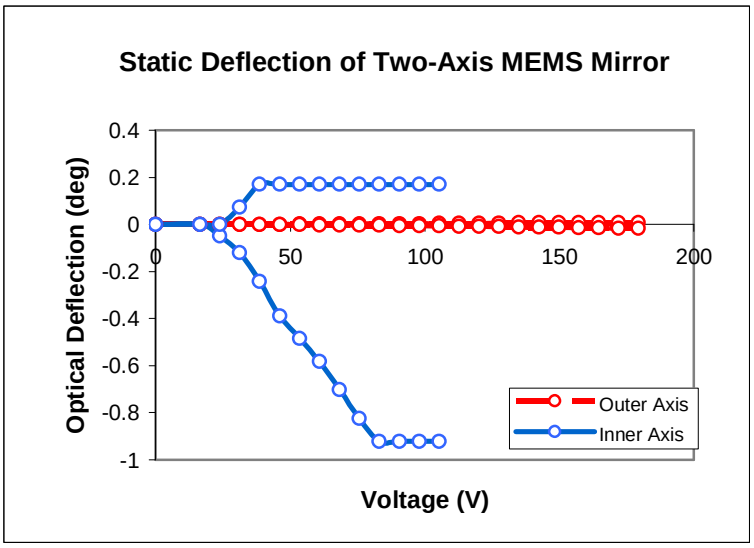

FIGURE 3.1.2.2. OPTICAL DEFLECTION OF THE MEMS MIRROR UNDER APPLIED DC VOLTAGE. Defects present in our device impaired static deflection.

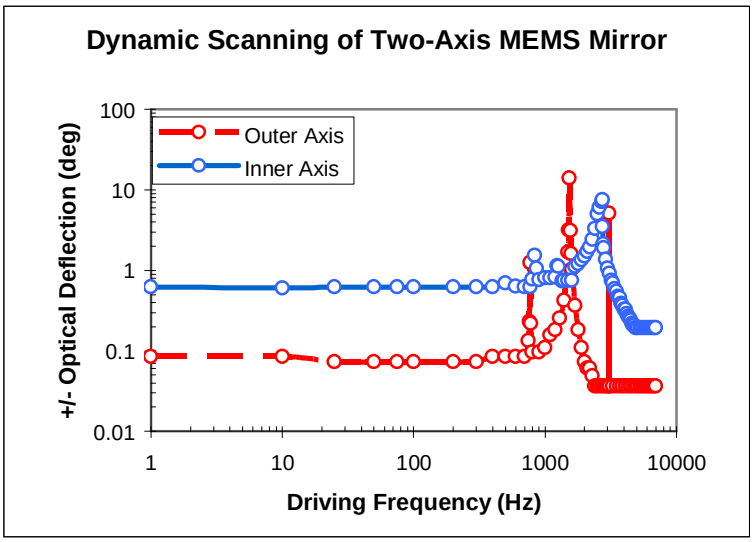

FIGURE 3.1.2.3. DYNAMIC SCANNING RESPONSE OF THE MEMS MIRROR BEFORE PACKAGING. Using a sinusoidal voltage signal, the mechanical resonance of the inner and outer axes could be excited, resulting in very large optical deflections at relatively low voltage. The peak voltage used here is 57 V. The resonant peaks occur at 2.73 kHz and 1.54 kHz for the inner and outer axes, respectively.

3.1.3: GRIN Objective Lens

Although the compact size and inexpensiveness of GRIN lenses make them attractive candidates for miniature TPM objective lenses, most applications have been unable to achieve diffraction-limited resolution. This has been attributed to the spherical and chromatic aberrations of the GRIN lens, which limit the lateral resolution to roughly twice that predicted by the diffraction limit [8].

Light rays traveling through a GRIN lens with a radial index of refraction gradient trace a cosine shape, shown in Fig 3.1.3.1, in which the number of periods traveled through the lens is referred to as the pitch. Most focusing lenses are slightly less than ¼-pitch, meaning that collimated light entering the lens is focused at the other side with some small working distance. A GRIN lens of precisely ¼-pitch focuses collimating

light on the exit surface of the lens. As a result, we chose to employ a 0.23-pitch GRIN lens, which, for a 1.8 mm outer diameter and 0.46 NA, possesses a working distance of 210 μm, sufficient to image most epithelial tissues. For plano-plano GRIN lenses of this size and pitch, numerical apertures greater than ~0.5 are not currently commercially available, and so this lens was chosen to obtain the tightest focusing.

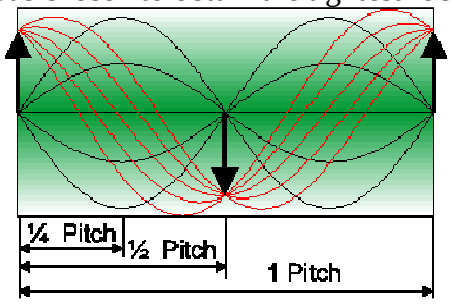

FIGURE 3.1.3.1. DEFINITION OF PITCH LENGTH IN A GRIN ROD LENS. The rod lenses used to collimate the laser light out of the PCF and also to focus the light as an objective lens at the sample were both 0.23-pitch lenses. Figure reproduced from [45].

To characterize the actual resolution of the 0.46-NA GRIN objective lens independent of other components of our miniaturized optical system, the GRIN objective lens was placed into a large-scale TPM system, shown in Fig. 3.1.3.2. We measured its lateral and axial point-spread functions (PSF) by imaging a sample consisting of 0.02% 100 nm fluorescent beads (Fluospheres, Molecular Probes) suspended in an agar gel, seen in Fig. 3.1.3.3. During this experiment, care was taken to ensure that the back aperture of the GRIN lens was filled and the excitation light was collimated to obtain the optimum resolution from the GRIN lens. Image analysis yielded lateral and axial PSFs with FWHM values of 786 ± 57 nm and 13.0 ± 1.6 μm, respectively, where the errors represent 95% confidence intervals and a sample size of 10 for both measurements. For comparison, the diffraction-limited FWHM values are 622 nm and 4.2 μm for lateral and axial resolution, respectively [6]. Here, the lateral PSF is 26% larger than the theoretical

diffraction limited value, much better than the 200% increase often cited in literature. The effect of aberrations is much more apparent in the increased axial PSF, however, and is very similar to measurements in other reports [8, 13, 35, 37]. These measurements provide a practical baseline performance for use of the GRIN objective in our miniaturized TPM system.

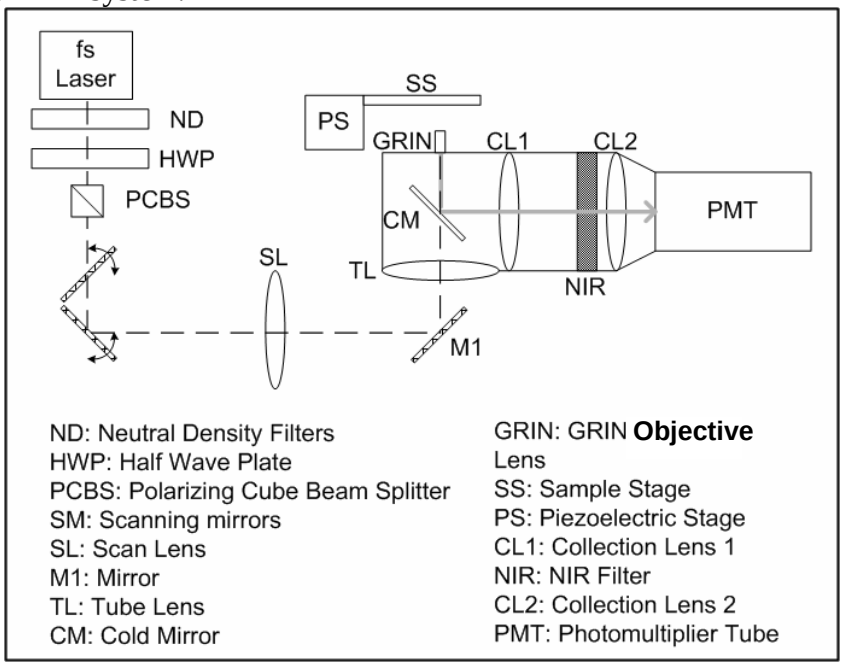

FIGURE 3.1.3.2. EXPERIMENTAL SETUP FOR CHARACTERIZATION OF GRIN OBJECTIVE LENS. Further details about the "table-top" TPM system can be found in Durr *et al.* [46].

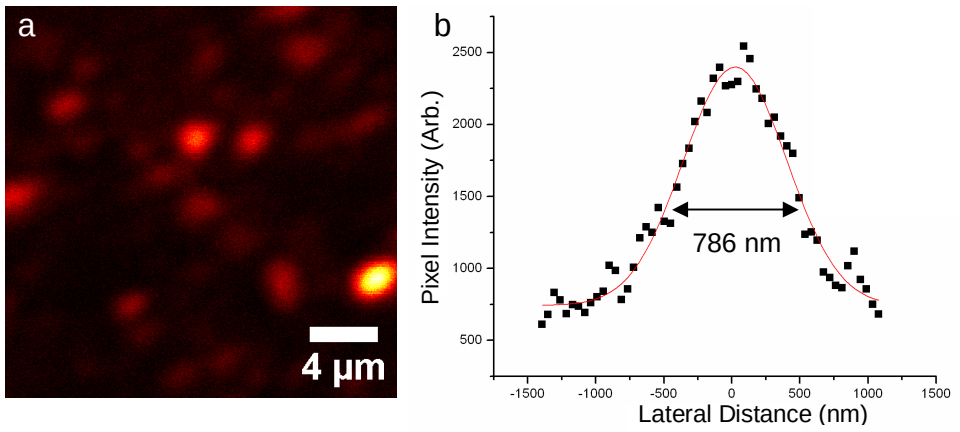

FIGURE 3.1.3.3. DETERMINATION OF THE GRIN LENS PSF. A solution of 100 nm fluorescent beads suspended in agar gel **a** as seen by two-photon microscopy through a 0.23-pitch, 1.8-mm diameter GRIN objective lens and **b** a representative PSF measured from these images. In **b,** the black dots represent measured intensity data and the red line is the Gaussian fit. Scale bar is 4 µm.

3.2: OPTICAL MODELING AND OPTIMIZATION

The optical system was modeled using sequential ray-tracing software (TracePro, Lambda Research) where collection efficiency and FOV were optimized. For analyzing the maximum potential FOV, a simplified imaging system was created using models of the aspherical lenses and GRIN objective lens that were chosen for use in the miniaturized probe, shown in Fig. 3.2.1. Scanning of the beam was simulated by varying the angles of collimated light with 0.34-mm $1/e^2$ diameter into the system and, for the measured maximum optical deflections of ±10.5° and ±10° for our MEMS device, the focal spot at the sample traced out a 380 µm × 360 µm FOV.

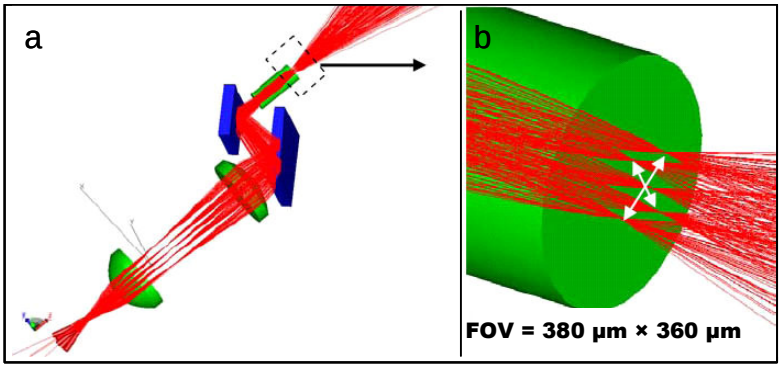

FIGURE 3.2.1 RAY-TRACING MODEL OF THE MINIATURE TPM/FLMS PROBE SYSTEM. a, the model of the system used for analysis of the FOV. **b**, a detailed view of the focal plane of the objective lens showing the predicted focal points at the maximum deflections of the MEMS mirror and the subsequent FOV.

Chapter 4: Probe Construction

The construction of the miniature probe inside a compact housing is discussed in this chapter. In addition, this chapter includes discussion of the data acquisition system constructed to control the MEMS scanning mirror and reconstruct the collected fluorescent signal into a coherent image.

4.1: PHYSICAL CONSTRUCTION OF THE MINIATURE TPM/FLMS PROBE

The individual components were combined in the miniature optical system shown in Fig. 4.1 and packaged in a probe housing machined from Delrin® acetal resin polymer. In the optical system, femtosecond laser pulses are delivered by 1 meter of air-core PCF and collimated by a 0.23-pitch GRIN lens with 1.8 mm diameter. A flip mirror is used prior to coupling of the laser light into the PCF to switch between imaging and microsurgery lasers. From the collimating GRIN lens, the laser light enters the housing and is scanned at 45° by the MEMS scanning mirror. The beam on the scanning mirror is imaged onto the back aperture of the GRIN objective lens (0.46 NA, 0.23 pitch, 210 µm working distance, 1.8 mm diameter) through the aspherical lens pair which also serves as a 3.4× beam expander. Fluorescence emission is collected by the 2-mm core plastic optical fiber, which is positioned directly behind a 5×5 mm^2 hot mirror with a cut-off wavelength of 715 nm. The collected fluorescence is delivered through 1 meter of the collection fiber and focused into a photomultiplier tube (H7422-40, Hamamatsu) by a 4 mm focal length lens with a Schott BG38 filter cutting scattered laser light.

Measuring at $10 \times 15 \times 40$ mm^3, the housing was machined using a computer numerical control (CNC) milling station, which facilitated rapid production of prototypes from a SolidWorks® computer model. Individual optical components are press-fit into the housing, as is a Delrin® lid which is used to seal the probe from stray light during use.

The use of press-fit grooves for positioning of the optical components allows for simple fabrication and assembly of prototypes during refinement of the design, however the lack of positioning control in the final housing (i.e. adjustment screws or micropositioners) limits the ability to adjust component alignment after fabrication of the housing. Further miniaturization of the design would likely require some sort of micropositioning solution to account for the added alignment sensitivity encountered in smaller optical systems.

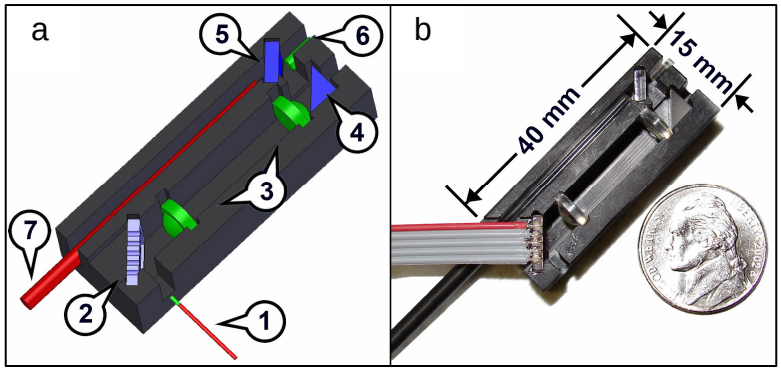

FIGURE 4.1.1. SCHEMATIC AND PHOTOGRAPH OF THE COMBINED TPM/FLMS PROBE. Description of the 10 × 15 × 40 mm^3 miniaturized two-photon microscope and femtosecond laser microsurgery probe. **a**, the model includes 1) air-core PCF, 2) two-axis MEMS scanning mirror, 3) miniature aspheric relay lenses, 4) mirror, 5) hot mirror, 6) 0.46-NA GRIN objective lens, and 7) 2mm-core plastic optical fiber. **b**, The photograph shows the miniature probe as built without the delivery fiber. The PCF and its collimating GRIN lens were mounted separately and aligned to the probe during experiments. The entire housing measures 10 × 15 × 40 mm^3, including a lid (not shown) which press fit onto the housing to protect the components and block stray light.

For imaging, the probe was mounted above the sample stage shown in Fig. 4.1.2 in an upright position, such that it pointed downward and imaged the sample from above.

The PCF and collimating lens were mounted in a separate mount held next to the probe housing.

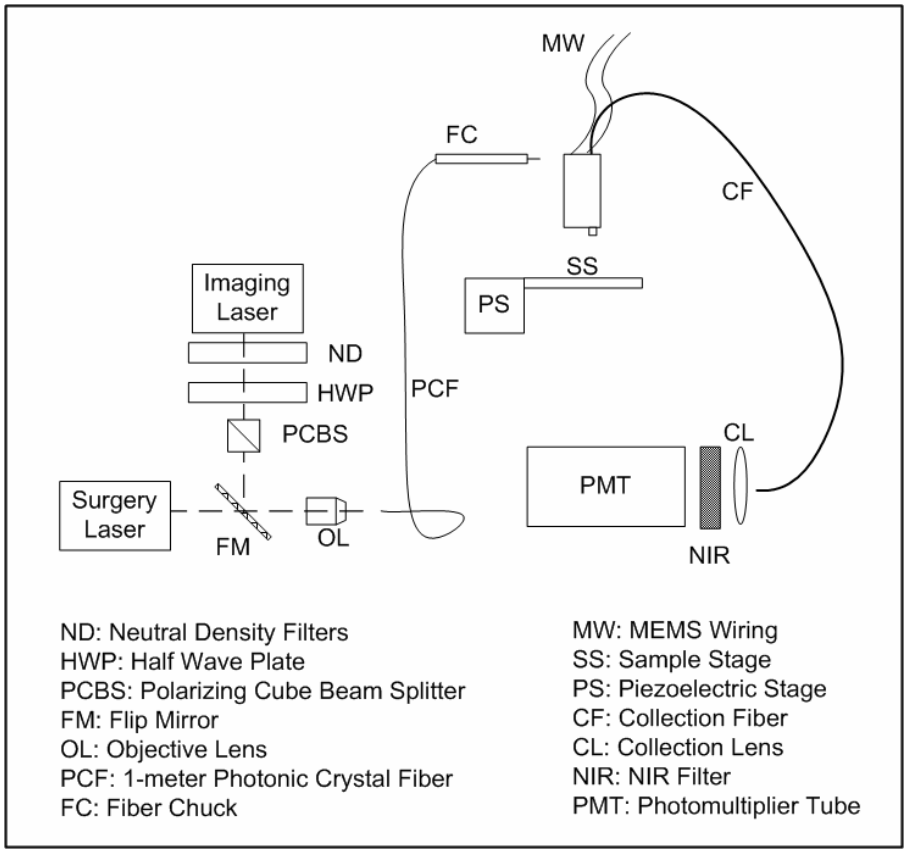

FIGURE 4.1.2. EXPERIMENTAL SETUP FOR THE COMBINED TPM/FLMS PROBE. A computer with data acquisition cards (not shown) was used to control the MEMS through the wiring shown and read the PMT signal from a preamplifier (not shown).

4.2: DATA ACQUISITION AND LISSAJOUS SCANNING

The PMT signal is amplified by a low-noise current preamplifier (SR570, Stanford Research Systems) operating in high-bandwidth mode and sampling at 1 MHz, or 1 μs per pixel. The amplified signal is then read into the computer through a data acquisition card (PCI-6115, National Instruments), which also shares duty with another data acquisition card (PCI-6711, National Instruments) for sending the driving signal to

the MEMS. This signal is amplified by a custom built 10-channel amplifier from AgilOptics before being delivered to the MEMS device.

Actuation of the MEMS scanning mirror and reconstruction of the imaging data w handled by a custom LabView® program. The program delivers sinusoidal voltage at the resonant frequencies of the MEMS scanning mirror through an amplifier to the MEMS device. The resulting motion of the MEMS mirror produces a Lissajous pattern, such as shown in Fig. 2.2.1b, which is imaged through the objective lens to scan the FOV at the sample. The Lissajous scanning pattern was chosen over the more conventional raster scanning pattern out of necessity. The raster scan requires one scanning axis to be moved far below resonance, where very little deflection was observed. Thus, to obtain sufficient deflection in both dimensions of the FOV, the Lissajous pattern was chosen. This provided the benefit of larger FOV, faster frame rate, and lower driving voltage than would have been otherwise possible, however.

When imaging with a Lissajous pattern, one may either define the frame rate as the rate at which the pattern repeats itself, which will be referred to as a "stable" pattern, or the frame rate may be set arbitrarily so that sequential frames are not scanned by the identical pattern, which will be referred to as an "unstable" pattern. The stable Lissajous pattern is most common and provides some advantages for image reconstruction, as the proper location of a pixel will be solely dictated by the order of the pixel in a given frame. Using this method, the frame rate is given by

$$\frac{f_x}{n_x} = \frac{f_y}{n_y} = f_R \qquad (2)$$

where f_x and f_y are two scanning frequencies, n_x and n_y are the smallest possible integers such that $n_x / n_y = f_x / f_y$, and f_R is the repeat rate or frame rate. For scanning frequencies with very large n values, this can lead to slow frame rates with certain pixels getting imaged many times per frame, while others may be imaged once or not at all. In

an unstable pattern, however, the frame rate is chosen independently of the scanning frequencies to compromise between fast frame rates, densely sampled frames, and few repeatedly sampled pixels. Because sequential frames are not scanned by the same pattern, pixels that are not sampled in one particular frame may be sampled in the subsequent frame. This is in contrast to a stable pattern, in which pixels that are not sampled in a single frame are never sampled, resulting in a lack of information for that location. The disadvantage of the unstable Lissajous scanning scheme is that the image reconstruction software must always track the relative deflection of the mirror for all points in time, so that each pixel can be assigned to the correct location in the reconstructed image.

In the miniature probe, an unstable Lissajous scanning scheme was used with the frame rate adjusted experimentally to balance high frame acquisition speed with good FOV coverage for a 256 × 256 pixel image. As implemented, pixels that are sampled more than once in a single frame are averaged. During imaging, it was found that a frame rate of 10 frames per second (fps) provided coverage of the FOV with few unsampled pixels. Higher frame rates were also investigated with rates as high as 20 fps still yielding little noticeable loss in information per frame. At these speeds, the human eye no longer detects "flicker" in between frames, indicating the potential of this system for near video-rate imaging.

The LabView® program also featured two imaging modes shown in Fig. 4.1.2a,b. In the first mode, the program displays each frame exactly as reconstructed using the given frame rate for near video-rate imaging of dynamic samples at low resolution. This imaging mode is well suited for real-time analysis of gross features with fast dynamics. In the second mode, the program displays a running average, where the current frame is averaged with the previous five frames. While this image still updates at the given frame

rate, it provides lower noise and greater detail as a result of the averaging and is best suited for finding regions of interest, visualizing slower dynamic processes, and examining samples with cellular-level detail. For the highest level of detail, larger numbers of frames are averaged during post-processing, and this function could be incorporated into the program for on-the-fly generation of high resolution still images. These images require a few seconds to take, depending on the number of frames used, and are ideal for imaging small scale sub-cellular features.

In one anticipated application of the probe, a clinician could begin imaging a patient using the "running average" mode to find the focal plane and seek out the region of interest. A suspicious area would then be examined in high detail with a long-averaged still for diagnosis. If necessary, the target could then be ablated using the high intensity laser, at which point a follow up image would confirm removal of the target.

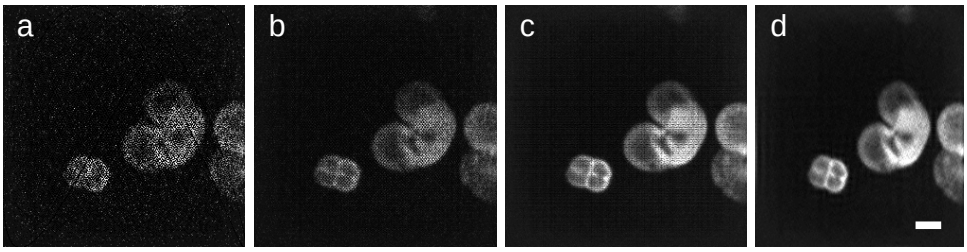

FIGURE 4.1.3. THE IMAGING MODES OF THE TPM/FLMS PROBE SOFTWARE. An example of a raw image frame of pollen grains is provided in **a**, which is indicative of frames that update at 10 Hz. A running average mode, **b**, is also available, in which the current frame is averaged with the 5 previous frames to provide greater detail. Though still updating at 10 Hz, this frame contains information from the previous 0.5 s. The frame in **c** consists of an average of 50 raw frames (5 s average) conducted during post-processing. Sub-resolution noise and zero-intensity pixels can be filtered out in post-

processing as well, along with calibration of the pixel dimensions, both of which are shown in **d**. Scale bar is 20 µm.

Further post-processing of the images was conducted using ImageJ version 1.37a software from the National Institutes of Health. Specifically, images were calibrated to the correct pixel dimensions and scaled to produce square pixels. The calibration method is described in Chapter 5. For presentation, a spatial filter was also applied using a fast Fourier transform (FFT) algorithm to eliminate spatial frequencies in the *x* and *y* directions greater than 1.2 cycles/µm [47, 48]. This was done to eliminate isolated pixels of zero intensity which were not sampled during the Lissajous scan and appear as sub-resolution black spots aligned in vertical and horizontal rows in the center of the image. The cut-off frequency for the filter was based on the measured resolution of the system, described in Chapter 5, so as to not filter out any useful signal. This is similar to the filtering implemented in Dickens *et al.*, where a digital FFT filter was used to remove the pixilation due to fiber spacing in a coherent fiber bundle endoscope [48].

Chapter 5: Probe Characterization

To experimentally determine the maximum extent and flatness of our FOV, a sample was prepared consisting of a 0.2% solution of 1 µm fluorescent beads suspended in water and evaporated onto a microscope slide. This sample provided a highly fluorescent and flat sample with which to characterize the field of view of the system. Images were taken using 8.2 mW average power at the sample as it was translated in x- and y-directions in 6 µm steps using piezoelectric stages, shown in Fig. 5.1a. Particle tracking software was then used to determine the number of pixels traversed for each step. This procedure was also conducted for all subsequent images acquired to ensure proper calibration. Using this procedure, a maximum FOV diameter of 310 µm was measured using peak MEMS driving voltages of 80 V to both axes. By varying the peak driving voltage from ~20 to 80 V, the FOV can be varied between 45 µm and 310 µm, although differences in voltage sensitivity between the mirror axes require unequal driving voltages for smaller FOVs. Figure 5.1a displays one of the images taken of this sample in which the collected intensity is seen to be fairly constant over much of the FOV, but then decrease rapidly at the edges. The vignetting, as well as the 14-18% decrease in maximum FOV with respect to the computer simulation, was found to be the clear aperture of the second relay lens in the beam path.

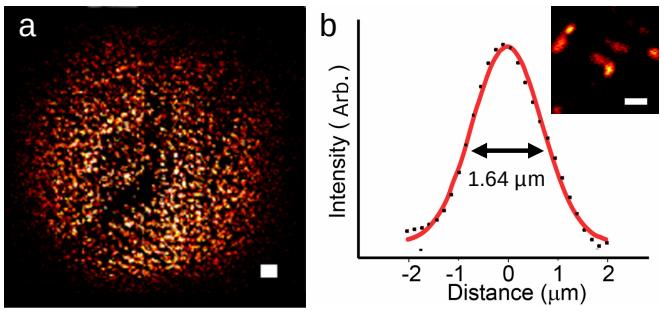

FIGURE 5.1. IMAGES OF FLUORESCENT BEADS USED TO CHARACTERIZE THE IMAGING CAPABILITIES OF THE TPM/FLMS PROBE. A glass slide covered in 1 µm beads, **a**, was used to characterize the maximum FOV, which is shown here to be 310 µm in diameter. To determine the PSF, 100 nm beads were suspended in agar gel, and their intensity profiles in *x*, *y*, and *z*, direction were measured. An example of the lateral PSF is provided in **b** where the black dots represent measured intensity and the red line is the corresponding Gaussian fit. An example image of a 100 nm bead taken with the probe is provided in the inset. Scale bar is 20 µm in **a** and 5 µm in **b**.

To determine FOV curvature and imaging resolution of the probe, another three dimensional sample was prepared consisting of 0.02% 100 nm fluorescent beads suspended in an agar gel, just as was used when determining the PSF of the GRIN objective lens in the table-top system. As seen in Fig. 5.1b, images of the 100 nm beads were used to experimentally determine the lateral point spread function (PSF) by fitting a Gaussian curve to the intensity profile across the center of a bead and measuring the full width at half maximum (FWHM). The axial resolution was measured similarly by measuring the intensity at the center of a bead as the focal plane was translated into the sample and again fitting a Gaussian curve to the profile. Each measurement was taken across 10 beads and reported errors correspond to the 95% confidence intervals about the mean. The measured lateral and axial resolutions of the probe were 1.64±0.17 µm and

16.4±2.0 µm, respectively. The lateral PSF measured in the probe is 109% larger than the corresponding PSF for the GRIN lens in the large scale table-top system, indicating that our resolution is limited by accumulation of aberrations and misalignment, rather than the resolving power of the objective lens. The axial PSF was only found to degrade by 26% in the probe, which suggests that the poor axial resolution compared to the diffraction-limited value is due primarily to the spherical aberration of the GRIN lens. The resolution was not observed to vary significantly throughout the FOV, indicating that the beam is well imaged to the back aperture of the objective lens for all scanning angles.

To demonstrate detailed imaging of biological samples, a prepared slide of mixed pollen grains (30-4264, Carolina Biological Supply Co.) was also imaged using the miniature system to demonstrate detail in biological samples. To ensure the full working distance of the lens could be used and reduce aberrations, the coverslip was removed from the sample before imaging. Figure 5.2a-d displays images of several distinct varieties of pollen grain where the differing morphologies are clearly observed.

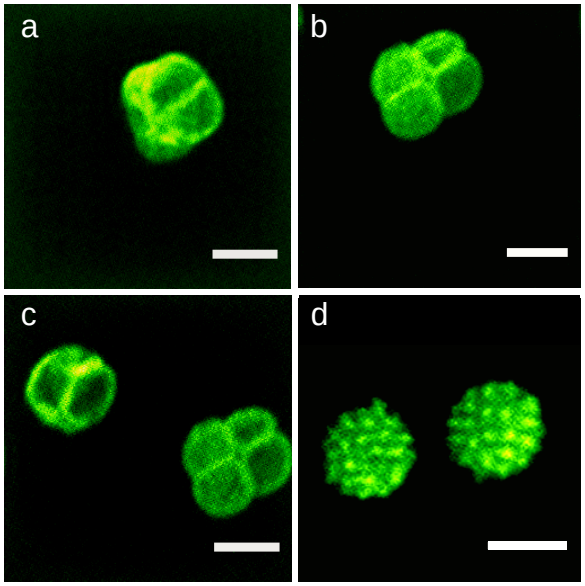

FIGURE 5.2. TWO-PHOTON FLUORESCENCE IMAGES OF FLUORESCENTLY STAINED POLLEN GRAINS TAKEN WITH THE MINIATURIZED PROBE. The images display a variety of morphologies illustrating the imaging capabilities of the probe. Each image represents a 50 frame average (5 s imaging time) and has been filtered by the FFT spatial filter described earlier. Scale bars are 20 µm.

Finally, the probe was used to image live cancer cells using a calcein acetoxymethyl (calcein AM) cell viability stain. To demonstrate live cell imaging, MDMBA468 breast carcinoma cells were prepared in complete L15 medium, and then rinsed and incubated for 30 minutes in 90 µM calcein AM. Calcein AM is cell permeable and is converted into fluorescent calcein by esterases in living cells. Imaging conducted immediately after incubation confirmed uptake and activation of the calcein, as indicated by a uniform fluorescence in all living cells. Figure 5.3 shows an image of the live cancer cells at 9 mW average power where cell structure and orientation can be determined; however intracellular detail is lost due to the strong cytoplasmic fluorescence of the calcein.

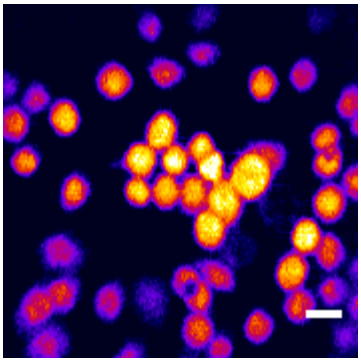

FIGURE 5.3. TWO-PHOTON FLUORESCENCE IMAGES OF BREAST CANCER CELLS LABELED WITH CALCEIN AM. This image is of a single layer of breast carcinoma cells that have been stained with the cell viability dye calcein AM. Image presented is a 50 frame average and was taken using 9 mW average power. Scale bar is 20 µm.

Chapter 6: Conclusion

In summary, the probe detailed here is a significant first step towards developing a clinical endoscope for combined two-photon fluorescence microscopy and femtosecond laser microsurgery. Measuring at 10 × 15 × 40 mm^3, the probe uses a combination of miniature optics and a MEMS scanning mirror to view areas up to 310 µm in diameter with 1.64 µm lateral resolution and at speeds of up to 10 frames per second. Comparing the imaging capabilities of the probe to the other published TPM probes, discussed in Chapter 1 and shown in Table 6.1, the system described here compares vary favorably in both frame rate and field of view. There is little variation amongst resolutions, however, as all the resolutions reported were achieved with similar GRIN optics.

Table 1. Summary of published two-photon microscopy probes.

Reference, Year	Resolution, lat. × ax. (µm)	FOV (µm)	Frame Rate (Hz)	Probe Size (mm)	Notes
[7], 2001	NR	140[1]	2	NR x 75.0	First published TPM probe. Used i*n vivo.*
[35], 2004	3.2 × 20.0	320	NR	1.0 × 1.0 × 7.8	Used fiber bundle.
[9], 2005	1.2 × 9.8	215	2	12.0 × 15.0 × 35.0	Motorized focusing mechanism.
[37], 2006	2.0 × 20.0	220	2.6	2.4 × 2.4 × NR	Spiral scanning of fiber.
[10], 2007	NR × 10.0	140 × 85[1]	0.03[2]	2.7 × 1.9 × 1.2	2-axis MEMS scanner.
[38], 2007	NR	80 × 20	5	11.0 × 19.0 × 20.0	2-axis MEMS scanner.
This work	1.6 × 16.8	310	10	10.0 × 15.0 × 40.0	Includes surgery laser.

NR = Not Reported. [1]Estimated from published images. [2]Estimated from reported 7 lines/second acquisition rate for 256 × 256 pixel image.

Furthermore, the potential for imaging of live cancer cells has been demonstrated and is a significant step towards imaging of tissue. To further explore the potential of this design as a combined imaging and microsurgery tool, the femtosecond laser ablation capabilities still need to be investigated. This will include both a systematic study of the ablation threshold in a well known media compared with the thresholds observed for

table-top systems, as well as demonstration of precise and controlled cellular ablation. This still presents significant challenges as the potential effect of the depolarization of the laser light by the fiber on the multiphoton ionization process is not well understood. In addition, with the current bare silicon MEMS mirror, only about 25% of the delivered laser power is reflected toward the sample, requiring higher laser powers entering the PCF. A means of delivering high laser powers without damaging the entrance tip of the PCF will need to be devised if the current system is to be used for high pulse energy ablation. Finally, long axial dimension of the focal volume, previously discussed in terms of the axial PSF, may present challenges from early plasma formation. Examples of such effects are plasma defocusing, where early low-density plasma formation changes the refractive index and acts as a negative focal length lens, and plasma shielding, where the reflectivity of the plasma prevents the absorption of part of the pulse energy. Care will need to be taken to work near the ablation threshold to mitigate these factors and tighter focusing from the probe objective may need to be developed.

Though capable of *in vivo* imaging as a surface probe in its current embodiment, future developments of this probe will include further miniaturization to allow for a wider range of biomedical applications. Additionally, a highly reflective metallic-coated MEMS mirror is being developed for increased pulse energy delivery and a higher NA objective lens will be included for better resolution. To fully utilize any increase in NA, however, the aberrations limiting the current system must be better understood and controlled. This will most likely necessitate the inclusion of a micropositioning system integrated into the probe housing to allow for on-the-fly alignment adjustments. Combined, these modifications will enable imaging of cellular autofluorescence and

tissue level microsurgery, both of which are critical to the clinical potential of the design. Though several issues remain to be addressed during adaptation into a clinical device, the optical design approach presented in this thesis shows great promise and could find applications in such disparate fields as dermatology, neurosurgery, and oncology.

References

1. U. K. Tirlapur and K. König, Nature 418, 290-291 (2002).

2. M. F. Yanik, H. Cinar, H. N. Cinar, A. D. Chisholm, Y. S. Jin, and A. Ben-Yakar, Nature 432(7019), 822-822 (2004).

3. A. Vogel, J. Noack, G. Hüttman, and G. Paltauf, Applied Physics B 81(8), 1015-1047 (2005).

4. W. Denk, J. H. Strickler, and W. W. Webb, Science 248(4951), 73-76 (1990).

5. P. T. C. So, C. Y. Dong, B. R. Masters, and K. M. Berland, Annual Review of Biomedical Engineering 2, 399-429 (2000).

6. W. R. Zipfel, R. M. Williams, and W. W. Webb, Nature Biotechnology 21(11), 1368-1376 (2003).

7. F. Helmchen, M. S. Fee, D. W. Tank, and W. Denk, Neuron 31, 903-912 (2001).

8. B. A. Flusberg, E. D. Cocker, W. Piyawattanametha, J. C. Jung, E. L. M. Cheung, and M. J. Schnitzer, Nature Methods 2(12), 941-950 (2005).

9. B. A. Flusberg, J. C. Jung, E. D. Cocker, E. P. Anderson, and M. J. Schnitzer, Optics Letters 30(17), 2272-2274 (2005).

10. L. Fu, A. Jain, C. Cranfield, H. Xie, and M. Gu, Journal of Biomedical Optics Letters 12(4), 0405011-04050113 (2007).

11. W. W. Webb, "Mpe physical principles" (November 7, 2007, 2003), retrieved November 7, 2007, 2007, http://www.drbio.cornell.edu/MPE/mpe1.html.

12. V. E. Centonze and J. G. White, Biophysical Journal 75(4), 2015-2024 (1998).

13. M. J. Levene, D. A. Dombeck, K. A. Kasischke, R. P. Molloy, and W. W. Webb, Journal of Neurophysiology 91, 1908-1912 (2004).

14. J. C. Jung, A. D. Mehta, E. Aksay, R. Stepnoski, and M. J. Schnitzer, Journal of Neurophysiology 92, 3121-3133 (2004).

15. M. Oheim, E. Beaurepaire, E. Chaigneau, J. Mertz, and S. Charpak, Journal of Neuroscience Methods 111, 29-37 (2001).

16. S. M. Ameer-Beg, P. R. Barber, R. J. Hodgkiss, R. J. Locke, R. G. Newman, G. M. Tozer, B. Vojnovic, and J. Wilson, Proceedings of SPIE 4620, 85-95 (2002).

17. E. B. Brown, R. B. Campbell, Y. Tsuzuki, L. Xu, P. Carmeliet, D. Fukumura, and R. K. Jain, Nature Medicine 7(7), 864-868 (2001).

18. P. Wilder-Smith, K. Osann, N. Hanna, N. El Abbadi, M. Brenner, D. Messadi, and T. Krasieva, Lasers in Surgery and Medicine 35(2), 96-103 (2004).

19. M. C. Skala, J. M. Squirrell, K. M. Vrotsos, J. C. Eickhoff, A. Gendron-Fitzpatrick, K. W. Eliceiri, and N. Ramanujam, Cancer Research 65(4), 1180-1186 (2005).

20. J. Leppert, J. Krajewski, S. R. Kantelhardt, S. Schlaffer, N. Petkus, E. Reusche, G. Hüttmann, and A. Giese, Neurosurgery 58(4), 759-767 (2005).

21. M. C. Skala, K. M. Riching, A. Gendron-Fitzpatrick, J. Eickhoff, K. W. Eliceiri, and J. G. White, PNAS 104(49), 19494-19499 (2007).

22. P. Carmeliet and R. K. Jain, Nature 407(6801), 249-257 (2000).

23. American Cancer Society. *Cancer facts & figures*, American Cancer Society, Atlanta, 2006.

24. V. Venugopalan, A. G. III, K. Nahen, and A. Vogel, Physical Review Letters 88(7), 0781031-0781034 (2002).

25. J. F. Ready, *Effects of high-power laser radiation* (Academic Press, New York, 1971), pp. 260-262.

26. A. Kaiser, B. Rethfeld, M. Vicanek, and G. Simon, Physical Review B 61(17), 11437-11450 (2000).

27. J. Noack and A. Vogel, IEEE Journal of Quantum Electronics 35(8), 1156-1167 (1999).

28. N. Shen, D. Datta, C. B. Schaffer, P. LeDuc, D. E. Ingber, and E. Mazur, Molecular and Cellular Biology 2(1), 17-25 (2005).

29. W. Watanabe, N. Arakawa, S. Matsunaga, T. Higashi, K. Fukui, K. Isobe, and K. Itoh, Optics Express 12(18), 4203-4213 (2004).

30. E. Zeira, A. Manevitch, A. Khatchatouriants, O. Pappo, E. Hyam, M. Darash-Yahana, E. Tavor, A. Honigman, A. Lewis, and E. Galun, Molecular Therapy 8(2), 342-350 (2003).

31. F. Bourgeois and A. Ben-Yakar, Optics Express 15(14), 8521-8531 (2007).

32. L. Sacconi, I. M. Tolic´-Nørrelykke, R. Antolini, and F. S. Pavone, Journal of Biomedical Optics 10(1), 014002-014001 - 014002-014005 (2005).

33. U. K. Tirlapur, K. König, C. Peuckert, R. Krieg, and K.-J. Halbhuber, Experimental Cell Research 263, 88-97 (2001).

34. J. B. Ashcom, R. R. Gattass, C. B. Schaffer, and E. Mazur, Journal of the Optical Society of America B 23(11), 2317-2322 (2006).

35. W. Göbel, J. N. D. Kerr, A. Nimmerjahn, and F. Helmchen, Optics Letters 29(21), 2521-2523 (2004).

36. J. C. Jung and M. J. Schnitzer, Optics Letters 28(11), 902-904 (2003).

37. M. T. Myaing, D. J. MacDonald, and X. Li, Optics Letters 31(8), 1076-1078 (2006).

38. W. Piyawattanametha, E. D. Cocker, R. P. J. Barretto, J. C. Jung, B. A. Flusberg, H. Ra, O. Solgaard, and M. J. Schnitzer, in *IEEE/LEOS International*

Conference on Optical MEMS and Nanophotonics, Hualien, Taiwan, August 12-16, 2007, 2007.

39. C. Xu and W. W. Webb, Journal of the Optical Society of America B-Optical Physics 13(3), 481-491 (1996).

40. M. Will, J. Limpert, T. Schreiber, F. Röser, S. Nolte, and A. Tünnermann, in *Photonics West/LASE*, San Jose, CA, 2005.

41. D. Lee and O. Solgaard, in *Proceedings of the Solid-State Sensors, Actuators and Microsystems Workshop, Hilton Head Island*, Hilton Head Island, South Carolina, June 6-10, 2004, 352-355.

42. L. Fu, A. Jain, H. Xie, C. Cranfield, and M. Gu, Optics Express 14(3), 1027-1032 (2006).

43. D. L. Dickensheets and G. S. Kino, Optics Letters 21(10), 764-766 (1996).

44. J. K. Ranka, A. L. Gaeta, A. Baltuska, M. S. Pshenichnikov, and D. A. Wiersma, Optics Letters 22(17), 1344-1346 (1997).

45. GRINTECH, GmbH, "Introduction to gradient index optics" retrieved December 1, 2007, http://www.grintech.de/.

46. N. J. Durr, T. Larson, D. K. Smith, B. A. Korgel, K. Sokolov, and A. Ben-Yakar, Nano Lett *7*(4), 941-945 (2007).

47. J. W. Goodman, *Introduction to fourier optics*, 3rd ed. (Roberts & Co., Englewood, 2005).

48. M. M. Dickens, M. P. Houlne, S. Mitra, and D. J. Bornhop, Optical Engineering 38(11), 1836-1842 (1999).

Vita

Christopher Luk Hoy was born in Bremerton, WA on September 21, 1982 to Jeffrey Craig Hoy and Elizabeth Willson Hoy. Christopher attended high school at James Madison High School in Vienna, VA, where he graduated in May of 2000. Subsequently, Christopher attended Virginia Polytechnic Institute and State University (Virginia Tech) where he graduated *cum laude* with a Bachelor's of Science in Mechanical Engineering, a concentration in Green Engineering, and a Minor in Mathematics in May of 2004. The following August, he enrolled in graduate school at The University of Texas at Austin, in Austin, Texas, where he lives with his two turtles.

Permanent address: 5004 Westfield Drive, Austin, Texas, 78731

This thesis was typed by the author.